Available online at www.sciencedirect.com
SCIENCE DIRECT®
Journal of the European Ceramic Society 25 (2005) 385–391
www.elsevier.com/locate/jeurceramsoc

Fracture behavior of cylindrical porous alumina with pore gradient

C. H. Chen*, K. Takita, S. Honda, H. Awaji

Department of Materials Science and Engineering, Nagoya Institute of Technology, Gokiso-cho, Showa-ku, Nagoya 466-8555, Japan

Received 11 November 2003; received in revised form 6 March 2004; accepted 13 March 2004
Available online 21 July 2004

Abstract

In this study, laminated cylindrical porous alumina materials with a pore gradient along the radial direction are fabricated by combining a lower sintering temperature with the presence of an organic-former (PMMA particles). It has been proved that pore morphology can be controlled by the lamination method in the centrifugal molding technique. The fracture behavior of the porous laminated alumina with a pore gradient is investigated by using the ring compression testing. An analytical formula to account for the pore gradient is introduced to calculate fracture strength based on the curved beam theory. There are two types of fracture behavior, which are not related to the lamination process and vary with the amount of pore-former. In the case of the same porosity, a reduction in fracture strength is observed with increase in the number of laminated layers, and the minimum strength is found in continuous graded cylinders.
© 2004 Elsevier Ltd. All rights reserved.

Keywords: Sintering; Porosity gradients; Microstructure-final; Fracture; Al_2O_3

1. Introduction

Porous ceramics are used as gas/liquid separators, catalyst supports and molecular sieves which can be used at high temperature and under severe chemical conditions. There are several approaches for the fabrication of porous ceramics in recent times, which can be mainly divided into the following four groups:[1] (1) controlling the particle size of ceramics to maintain constant pores among particles; (2) reducing the forming pressure and/or sintering temperature; (3) mixing the ceramic powders with a bubble former where the large and homogenous pores can be introduced; and (4) mixing ceramic powders with additional organic particles, which vaporize at relatively low temperatures and form small and homogenous pores. The microstructure of porous ceramics retains sufficient strength and imparts gas/liquid permeability, which enables the product to serve as gas/liquid separators and catalyst supports.

In this study, cylindrical porous ceramic tubes with a pore gradient are fabricated by combining a lower sintering temperature with the presence of an organic pore-former by centrifugal molding technique. It is attempted to use the inner part as the support, which should be mechanically strong and offer good permeability, and the outer part as the separation media due to the pore gradient of the cylinder.[2] Functionally gradient hollow cylinders were also fabricated by using the centrifugal molding technique, which uses the difference in the centrifugal force acting on powder mixtures to create a gradient compositional distribution along the radial direction due to the difference in the mixture densities and particle sizes.[3] The formation of tubes with homogenous microstructure or with separated microstructure can be controlled by adjusting the slurry character.[4] The scope of this work is to develop and characterize laminated cylindrical porous alumina with a pore gradient. The behavior of laminated rings cut from the tubes subjected to ring diametral compression testing is investigated. A new analytical formula to account for the pore gradient is introduced based on the curved beam theory.

2. Experimental procedure

Alumina powder (AES-12, Sumitomo Chemical Co.) with particle size averaging 0.5 μm, and poly methyl metha acrylate (PMMA) powder as pore-former with particle size averaging 10 μm were taken as the starting materials. PMMA particles are the desirable pore-former due

* Corresponding author. Tel.: +81-52-735-5276; fax: +81-52-735-5276.
E-mail address: chunhong@zymail.mse.nitech.ac.jp (C.H. Chen).

0955-2219/$ – see front matter © 2004 Elsevier Ltd. All rights reserved.
doi:10.1016/j.jeurceramsoc.2004.03.016

Table 1
PMMA contents of the laminated samples

Number	Laminate numbers	PMMA content (vol.%)				
		1	2	3	4	Total
4N1	4	0	5	15	20	10
4N2	4	0	15	25	40	20
4N3	4	5	10	15	20	10
4N4	4	10	15	25	30	20
4N5	4	15	25	35	45	30
3N1	3	0	10	20	–	10
3N2	3	0	20	40	–	20
3N3	3	5	10	15	–	10
3N4	3	10	20	30	–	20
3N5	3	15	30	45	–	30
2N1	2	0	20	–	–	10
2N2	2	5	15	–	–	10
2N3	2	15	25	–	–	20
2N4	2	20	40	–	–	30

to their homogenous particle sizes and low vaporization temperature.[5] For good dispersion, dispersant Seruna D-305 (Chokyoyushi Co., Japan) was added with distilled water as solvent. Ball clay (Seto, Japan) as the binder was added with 0.5 mass% to enhance the green strength during handling. 0.25 mass% of MgO was added as the sintering aid and grain growth inhibitor.

The powders mentioned previously were first mixed in a dispersant solvent by magnetic stirring for 1 h. Then the mixed slurry was treated ultrasonically to break down particle agglomerates. Finally the slurry was deaired in a vacuum for 15 min before final molding. Each slurry with different volume percentage of PMMA particles was prepared with the aim of producing the same layer thickness. The PMMA particles used in each slurry increase linearly from the outer to the inner walls as shown in Table 1. Then the slurry was poured in the stainless steel mold with inner diameter of 20 mm and the length of 70 mm. For easy removal of the sample after drying, the inner surface of the mold was pre-coated with a vaseline as lubricant. The cylindrical mold was centrifuged along the radial direction with a speed of 3000 rpm for 15 min. The residual liquid was poured out after centrifugation and the slurry for forming the next layer was poured in the mold, the same procedure was repeated. Slurry viscosity was adjusted to avoid the inhomogeneous properties in each laminate. The green tubes finished were dried vertically inside the mold in a vacuum chamber to maintain the shape. The temperature was allowed to rise to 100 °C with a ramp of 10 °C/h. The tubes shrunk and released easily from the mold during drying. The pore-former PMMA was dissociated completely by the slow heating rate 30 °C/h and the hold of 1 h at 500 °C. The green tubes were sintered at 1350 °C for 1 h in air.

The density and porosity of the sintered tubes were measured by the Archimedes method with distilled water as a media. Microstructures of the sintered specimen were examined to determine pore gradients by Scanning Electron Microscope (SEM) on the cross-sectional surfaces in equal intervals from the inner to the outer walls. For mechanical evaluation, the tubes were cut into 5 mm in length by diamond cutter and tested under ring diametral compression testing with a mechanical testing machine (Instron 5582, Japan) with a crosshead speed of 0.5 mm/min. The compression strength of the tubes was determined following the standard testing method (JIS Z 2507) for diametral compression.

3. Stress distribution under ring diametral compression

To obtain the stress distribution of graded ring specimen with a rectangular cross section subjected to diametral compression testing, the hoop strain ε_θ and hoop stress σ_θ are considered by the theory of pure bending of the curved bar.[6] It is clear that a feature of the curved beam theory is the non-uniform nature of the deformation; such as the strain and stress at a given point depend on the location of the point with respect to the neutral axis of the specimen. The transverse cross-sections of the beam, which are originally plane and normal to the center line, will remain unaltered after bending according as per this theory. The strain ε_θ at any radius r on any radial plane of angle ϕ is given by:

$$\varepsilon_\theta = \frac{\varepsilon_0\rho + y\omega}{\rho + y} \tag{1}$$

where ε_0 is a strain at a centroid, ρ is the radius of the center axis, y is the layer distance from the center line and ω is the angular strain.

Then the stress in the ring at the distance y is as follows:

$$\sigma_\theta = E(x)\varepsilon \tag{2}$$

where x is the non-dimensional distance along the radial direction and $E(x)$ is the radial gradient of Young's modulus.

To determine two unknowns ε_0, ω in Eq. (1), two static conditions are used and expressed as:

$$N = \int_A \sigma_\vartheta \mathrm{d}A = \varepsilon_0 \int_A \frac{\rho}{\rho + y} E(x)\mathrm{d}A + \omega \int_A \frac{y}{\rho + y} E(x)\mathrm{d}A \tag{3}$$

$$M = \int_A \sigma_\vartheta y \mathrm{d}A = \varepsilon_0 \int_A \frac{\rho y}{\rho + y} E(x)\mathrm{d}A + \omega \int_A \frac{y^2}{\rho + y} E(x)\mathrm{d}A \tag{4}$$

where A denotes the area of the cross section. For convenience, the following symbols are used.

$$C_1 = \int_A \frac{\rho}{\rho + y} E(x)\mathrm{d}A$$

$$C_2 = \int_A \frac{y}{\rho + y} E(x)\mathrm{d}A$$

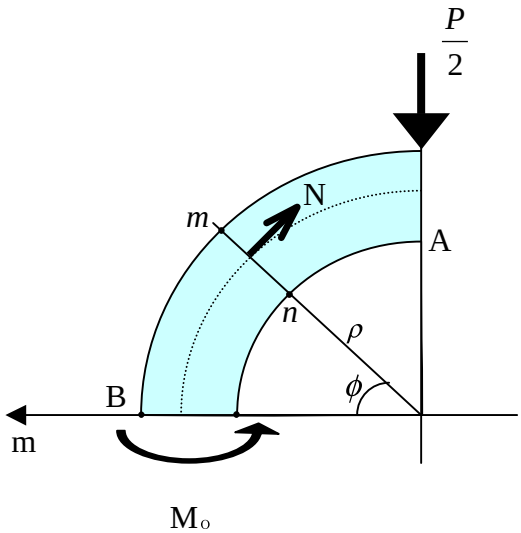

Fig. 1. Schematic illustration of the diametral compression testing for 1/4 O-ring.

$$C_3 = \int_A \frac{\rho y}{\rho + y} E(x) \mathrm{d}A$$

$$C_4 = \int_A \frac{y^2}{\rho + y} E(x) \mathrm{d}A$$

Solving Eqs. (3) and (4), ε_0 and ω can be expressed:

$$\varepsilon_0 = \frac{C_4 N - C_2 M}{C_1 C_4 - C_2 C_3} \tag{5}$$

$$\omega = \frac{C_1 M - C_3 N}{C_1 C_4 - C_2 C_3} \tag{6}$$

The 1/4 O-ring is considered as shown in Fig. 1, because the deformation of the ring in a diametral compression testing is symmetrical about a diameter. The axial load N and the moment M at any radial plane of angle ϕ are balanced with the applied load P and are given by the following equations:

$$N = -\frac{P}{2} \cos \phi \tag{7}$$

$$M = M_0 - \frac{P\rho}{2}(1 - \cos \phi) \tag{8}$$

where M_0 is a statically indeterminate moment working on the cross-section $m - n$ to maintain no rotation together with the axial load.

If the axial force N, shear stress F, and moment M are applied to the small element $A \times \mathrm{d}s$, the strain energy stored in the body is $\mathrm{d}U_N$, $\mathrm{d}U_F$, $\mathrm{d}U_M = 0.5M\Delta\mathrm{d}\phi$, respectively. Also, because the work done ($\mathrm{d}U_{MN} = N\varepsilon_0 \mathrm{d}s$) by the axial load is carried out based on the strain of centroid coming from the bending moment M, the work is added to the strain energy. Therefore, the total strain energy stored in the 1/4 O-ring can be expressed:

$$U = U_N + U_M + U_{MN} + U_F \tag{9}$$

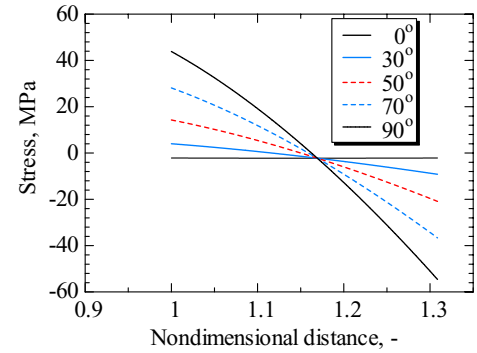

Fig. 2. The stress distribution of 1/4 O-ring under the diametral compression testing.

The strain energy of shear stress is so little that it can be ignored compared to that of the others. Moreover, cross-section $m - n$ does not rotate when it receives bending. Therefore, the angular strain i_0 of cross-section $m - n$ becomes zero and is written referring to the Castigliano's First Theorem,[7] as follows:

$$i_0 = \frac{\mathrm{d}U}{\mathrm{d}M_0} = 0 \tag{10}$$

Integrating Eq. (9) with respect to r:

$$\frac{\mathrm{d}U}{\mathrm{d}M_0} = \frac{\mathrm{d}U_N}{\mathrm{d}M_0} + \frac{\mathrm{d}U_M}{\mathrm{d}M_0} + \frac{\mathrm{d}U_{MN}}{\mathrm{d}M_0} = 0 \tag{11}$$

The items of Eq. (11) can be obtained by several integrals. The constant M_0 in the cross-section $m - n$ is given as following:

$$M_0 = \frac{-(P\rho/2)(2C_1 - \pi C_1 + (C_3/\rho) + 2C_2)}{C_1 \pi} \tag{12}$$

Stress–strain distribution field of a graded ring subjected to the diametral compression testing is thus determined using a numerical calculation scheme.

The typical stress distribution is shown in Fig. 2, where X-axis is the non-dimensional distance along the radial direction and Y-axis is the stress under the diameteral compression testing. It is observed that there is a maximum where the non-dimensional distance is 1 and at any radial plane of angle ϕ is 90°. That is, the maximum stress is applied to the inside of the ring along the load axis and can be regard as the fracture strength of the ring based on the maximum hoop stress theory of fracture criterion.

4. Results and discussion

4.1. Microstructure and composition

The laminated porous tubes prepared are shown in Fig. 3. No defects, like delamination or crack are observed after sintering, though the thermal mismatch stress occurs due to the different properties of each laminate. It means that

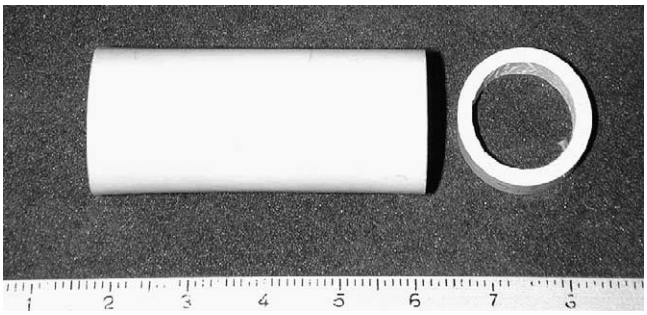

Fig. 3. Specimen of the laminated porous tube.

a good packing structure is obtained by the lamination method. Continuous SEM micrographs of specimens with three laminated layers (3N2, 3N3) are shown in Fig. 4, where there are high porosity on the inner wall and low porosity on the outer wall of the tubes. Pores appear as black phase. The figure shows the pore morphology of specimens is easy to be controllable using the lamination method. PMMA particles distribute uniformly in alumina matrix in each laminate. The interface of each laminate in sample 3N2 is shown in Fig. 5. It is clear that in each laminate, there is the large difference in the number of pores formed by the PMMA particles. However, no defects, such as detachment and crack, exist between layers because the pore agglomeration is seldom visible by distributing PMMA particles uniformly in each laminate. Fig. 6 shows the microstructure of the laminate without PMMA. The results indicate that the grain growth of alumina particles is not observed and

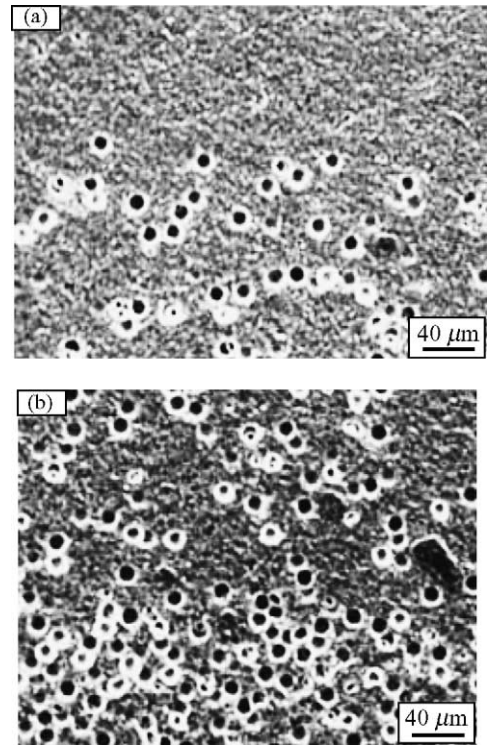

Fig. 5. SEM micrographs of the interface in specimen 3N2, (a) the interface between the laminate without PMMA particles and the laminate with 20 vol.% PMMA particles, (b) the interface between the laminate with 20 vol.% and the laminate with 40 vol.% PMMA particles.

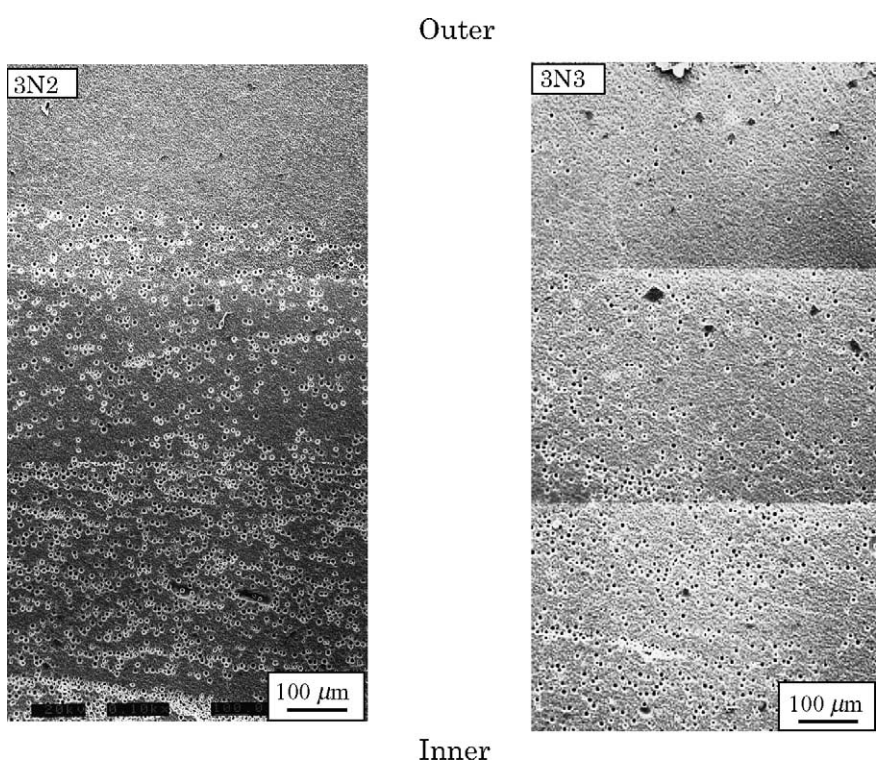

Fig. 4. SEM micrographs of the specimens 3N2 and 3N3.

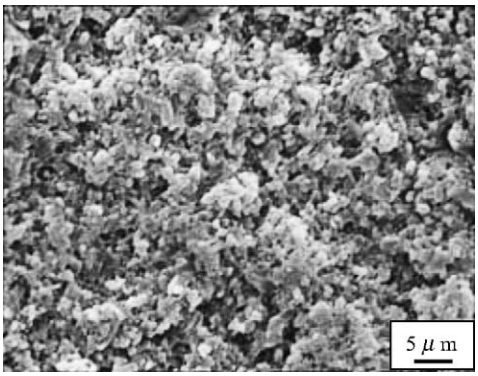

Fig. 6. SEM micrograph of the laminate without PMMA particles.

continuous but sub-micron pores, as open pores, are predominant in alumina samples sintered at lower temperature.

Fig. 7 shows the microstructure of one laminate for specimen 3N2 and 3N3 with 10 and 40% PMMA additions by volume. On the addition of the pore-former PMMA, spherical pores with 10 μm in diameter could be clearly observed. In the case of 10 vol.% PMMA, the spherical pores are connected with a sub-micron pore though each spherical pore exists independently of the others. In the case of 40 vol.% PMMA, the spherical pores were observed uniformly in the alumina matrix to form a three-dimensional network and also to serve as open pore regardless of the sub-micron porosity.

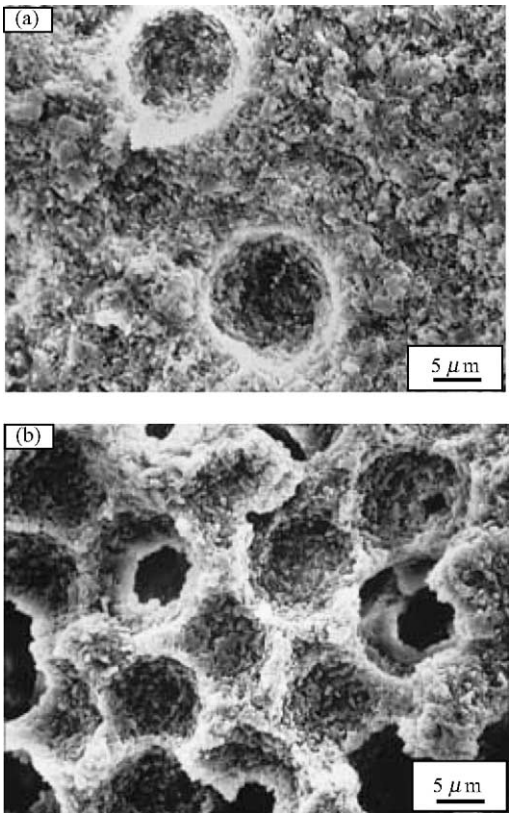

Fig. 7. SEM micrographs of the laminates with PMMA particles, (a) the laminate with 10 vol.% PMMA particles, (b) the laminate with 40 vol.% PMMA particles.

4.2. Fracture behavior

The results after the ring diametral compression testing were roughly classified into two types based on the load versus load-point displacement curves as shown in Fig. 8.

The failure appearance of type I is shown in Fig. 9, where (a) is after complete failure, (b) is immediately after the first maximum peak a. The results show the peak a in Fig. 8(a) corresponds to the initiation of a crack at the inner surface A shown in Fig. 1, which extends into the exterior along the load axis, resulting in two c-shaped pieces with linear crack growth. At peak b, cracks are developed on the outer surface B shown in Fig. 1 and propagate into the interior perpendicular to the load axis, i.e. the schematic failure mode of type I may be expressed in Fig. 10, where there is a very good agreement with Itoh et al.[8] and Matushima et al.[9]

The failure appearance of type II is shown in Fig. 11. It is found that peaks a and b indicate the initiation of crack on the inner and outer surface A and B. The crack deflection is seen clearly along the load axis, which corresponds with peak c. That is, the crack is arrested when a pore from PMMA agglomerate exists on the crack growth path, and, the crack was deflected along the periphery of the pore after the increase in load to peak c.

Therefore, the inner strength of O-ring specimens can be calculated by combining analyses formula mentioned-above with the first peak a in both types. The experiments show

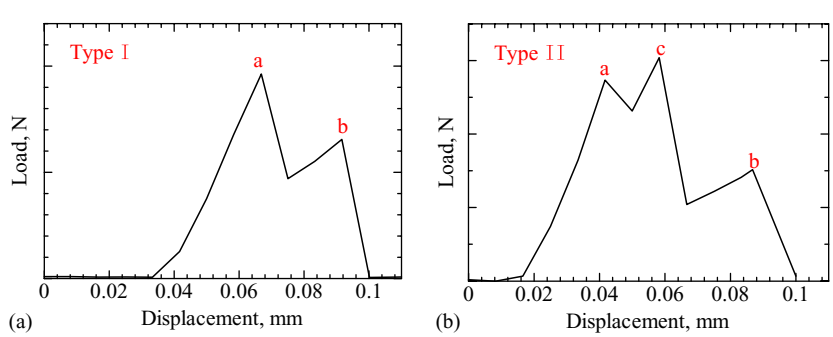

Fig. 8. Two types after the ring diametral compression testing.

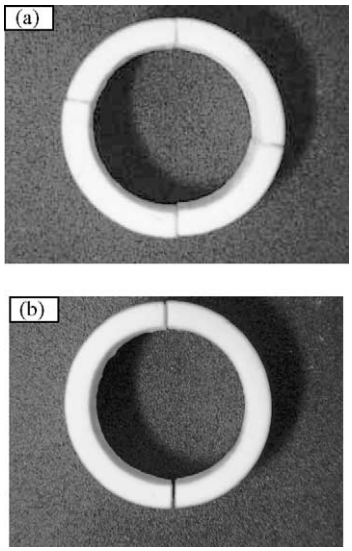

Fig. 9. Failure appearance of Type I, (a) after complete failure, (b) after the first maximum peak.

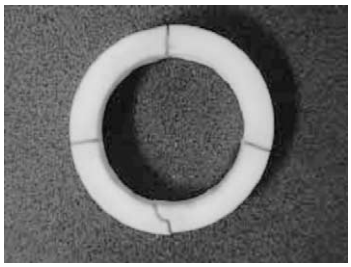

Fig. 11. Failure appearance of type II.

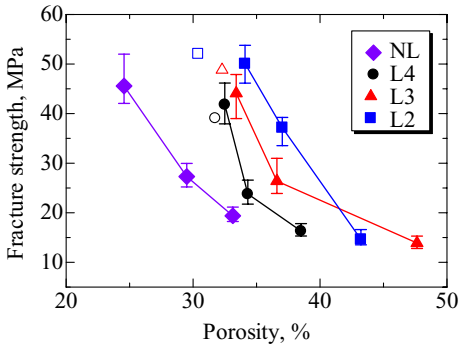

Fig. 12. Fracture strength vs. porosity of laminated types and continuous types.

that with increase of PMMA additions, type I of fracture behavior becomes type II gradually, which shows that this phenomenon is not related to the lamination process. The behavior differs from that of laminated SiC tubes produced by electrophoretic deposition, where the graphite layers are set into SiC laminate.[10]

4.3. Diametral compression strength

The distribution of Young's modulus along the radial direction was obtained from the pore gradient.[11] The fracture strength can be calculated based on the analysis mentioned in Section 3. The relations between the fracture strength and porosity are shown in Fig. 12 for continuous types (NL) and laminated types, where specimens are divided into three groups (L4, L3, L2) by the laminate number. PMMA amount varies from 10, 20, and 30% by volume in each specimen. The hollow symbols indicate the laminated types containing an alumina single layer on the outer side, where the total PMMA amount is 10 vol.%. It is observed that the porosity of specimen with the same PMMA additions varies with the number of laminate layers. With decrease in the number of laminate layers, the porosity is gradually increased for great benefit to the air permeability. However, it must be realized that when the volume variation of PMMA particles between two layers is larger than 20, some defects may appear. An almost similar trend for fracture strength versus the volume fraction porosity occurs in specific porosity region, which is shifted closer to high porosity with decrease in the number of laminated layers. The fracture strength is decreased with the increase of the PMMA amount in all specimens. In the case of the same porosity, a reduction in fracture strength

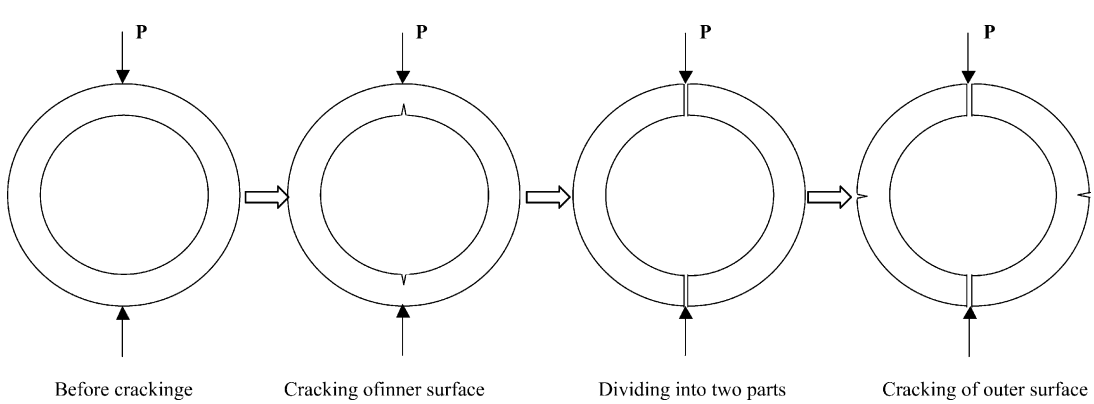

Fig. 10. Schematic failure mode of type I.

is observed with increase in the number of laminated layers, and the minimum strength is observed in continuous graded tubes. It is because the PMMA contents in the inner wall of tubes increase as shown in Table 1, and the radial gradient of Young's modulus introduced in Eq. (2) varies with the number of laminated layers. The experimental results show that the fracture strength and porosity are easy to be controllable by selecting the number of laminated layers and PMMA distributions in each layer. The error of fracture strength with high porosity is less than that with low porosity regardless of the laminated layers.[12] The reasons could be that fracture origin is limited in the spherical pore formed by PMMA particles.

5. Conclusions

Laminated cylindrical porous alumina samples with a pore gradient were fabricated. It has been proved that the pore morphology along the radial direction can be controlled by the lamination method in centrifugal molding technique. A ring diametral compression testing has been performed to investigate fracture behavior of porous ceramics with a porosity gradient. The theoretical model is introduced to analyze fracture strength based on the curved beam theory. The results show fracture behavior varies with the amount of pore-former, regardless of the laminated layers. In the case of the same porosity, a reduction in the fracture strength is observed with increase in the number of laminated layers, and the minimum strength is found in continuous graded cylinders.

References

1. Ishizaki, K., Komarneni, S. and Nanko, M., *Porous Materials—Process Technology and Applications*. Kluwer Academic Publishers, The Netherlands, 1998, Chapter 2.
2. Chao, W. J. and Chou, K. S., Studies on the control of porous properties in the fabrication of porous supports. *Key Eng. Mater.* 1996, **115**, 93–108.
3. Sivakumar, R., Nishikawa, T., Honda, S., Awaji, H. and Gnanam, F. D., Processing of mullite-molybdenum graded hollow cylinders by centrifugal molding technique. *J. Eur. Ceram. Soc.* 2003, **23**(5), 765–772.
4. Chen, C. H., Honda, S., Nishikawa, T. and Awaji, H., A hollow cylinder of functionally gradient materials fabricated by centrifugal molding technique. *J. Ceram. Soc. Jpn.* 2003, **111**(7), 479–484.
5. Nishikawa, T., Nakashima, A., Honda, S. and Awaji, H., Effects of porosity and pore morphology on mechanical properties of porous alumina. *J. Soc. Mater. Jpn.* 2001, **50**(6), 625–629.
6. Timoshenko, S. and Young, D. H., *Elements of Strength of Materials* (*4th ed.*). D. Van Nostrand Company, Inc., 1962, Chapter VI.
7. Ford, H. and Alexander, J. M., *Advanced Mechanics of Materials*. Longmans, Green and Co. Ltd., 1963, p. 350.
8. Itoh, Y., Ikeda, M. and Suyama, S., Fracture behavior of ceramic filter using Diametral Ring Compression Test. *J. Ceram. Soc. Jpn.* 1999, **107**(12), 1196–1200.
9. Matushima, Y., Kitaoka, S., Awaji, H., Chen, C. H., Cao, J., Nanjo, F. *et al.*, Thermal cyclic fatigue of porous ceramics for hot gas filters. *J. Soc. Mater. Jpn.* 2002, **51**(6), 622–627.
10. Vandeperre, L. J. and Van Der Biest, O. O., Graceful failure of laminated ceramic tubes produced by electrophoretic deposition. *J. Eur. Ceram. Soc.* 1998, **18**, 1915–1921.
11. Nishikawa, T., Honda, S. and Awaji, H., Characterization of cylindrical porous ceramics prepared with centrifugal molding. *Ceram. Trans.* 2002, **133**, 171–176.
12. Nanjangud, S. C., Brezny, R. and Green, D. J., Strength and Young's modulus behavior of a partially sintered porous alumina. *J. Am. Ceram. Soc.* 1995, **78**, 266.